Narrowband Terahertz Emission With Tunable Orbital Angular Momentum by Vortex Laser-Beam Interaction

Haoran Zhang [ID], Wenxing Wang, Cheng Li, Zixin Guo, Zhigang He, Shancai Zhang, Qika Jia [ID], and Lin Wang

Abstract—**Terahertz vortex beams need to be developed for supporting new applications in fundamental sciences. In this paper, a novel and feasible scheme is presented for generation of helically microbunched electron beam for the emission of terahertz (THz) vortex pulses. In the scheme, a seed laser pulse with longitudinal and azimuthal modulation is firstly produced by optical beating of dual-vortex pulses. Through the laser-electron interaction, such a complex profile of laser can be converted to a periodically azimuth-dependence energy modulation in the electron beam, which finally forms a helical microbunching structure in the beam after a dispersion section. Then, this electron beam is applied to emit THz vortex beams and its quantum number can be continuously tuned by changing the topological charges of the optical laser pulses. This approach is suited to conventional accelerator system consisted of a modulator and a chicane. We expect this presentation can access to new researches in THz science.**

Index Terms—**Electron beams, particle beam handling, terahertz radiation, undulators.**

I. INTRODUCTION

FROM the fundamental point of view, radiation sources with high-order transverse modes are among intensively studied topics in optics [1]. These light vortices, which are carrying orbital angular momentum (OAM) equivalent to $\hbar l$ per photon, have a field dependence of $exp(il\phi)$, where ϕ is the azimuthal coordinate perpendicular to the wave propagation direction and l is an integer referred to the topological charge or quantum number.

With phase singularity and a degree of freedom with infinite number of eigenstates, vortex light brings strong interests in many practical applications, such as, communication [2], microscopy [3] and micromanipulation [4]. Moreover, the vortex beams with different wavelength can trigger some special and novel phenomena. Vortex beams at short wavelength have promising applications in magnetic circular dichroism [5],

photoionization experiments [6] and resonant inelastic x-ray scattering [7]. Extending to long wavelength in the terahertz (THz) region, photons can be effective to excite the quasi-particles and collective interactions at molecular level [8]. THz vortex beams are also very attractive to a variety of fundamental and applied sciences and has been applied to spectroscopy of magnetic excitations [9]. It can couple to magnetism exhibiting dichroisms and this effect for vortex beam is more pronounced than that for circularly polarized light. Further, Sirenko *et al.* utilized the higher-order THz vortex beams with OAM of $l = \pm 2, \pm 3, \pm 4$ in combination with a spin angular momentum (SAM) of $\sigma = \pm 1$ to explore the selection rules for absorption of vortex beams at the antiferromagnetic resonances [10]. It can be useful in studying collective excitations in magnetic solids, and the coupling between THz vortex beams with high orders of the total angular momentum may provide application for studies of nonlocal collective spin and carrier excitations in quantum systems. Hence, THz vortex sources urgently need to be developed as a powerful complement of THz photonics, extending to relative scientific researches.

Although the optical-based methods to generate vortex beams in the infrared and visible spectral regions have been fully developed [11]–[13], production of intense THz vortices still remains a challenge. The THz vortex can be directly structured from THz Gaussian beams by phase modulation, including spiral phase plates [14], computer-generated holograms [15], metasurfaces [16], liquid crystals [17], etc. Especially, the derivatives of liquid crystal can bring some versatile functions [18], [19]. However, these methods are limited by mode conversion efficiency due to low transmittance. Specially, a polymeric Tsurupica spiral phase plate can achieve a efficiency of over 50% due to the low dispersion and high transmission in the THz region [20], [21]. Yet, it only can be adopted in a certain frequency. Moreover, THz vortex beams can be indirectly generated by optical vortex-pumped difference frequency generation (DFG) in a nonlinear crystal [22], [23] or vortex-laser-induced air plasma [24], [25].

Modern accelerator facilities can deliver high-brightness optical beams covering a quite wide spectrum. It's a good choice to directly transfer the normal accelerator-based radiations to the high-order modes, but the wavelength and power are limited by the damage threshold of the external optical mode conversion elements. Start with Sasaki's work [26], [27], direct vortex radiations based on the accelerator regime have been studied.
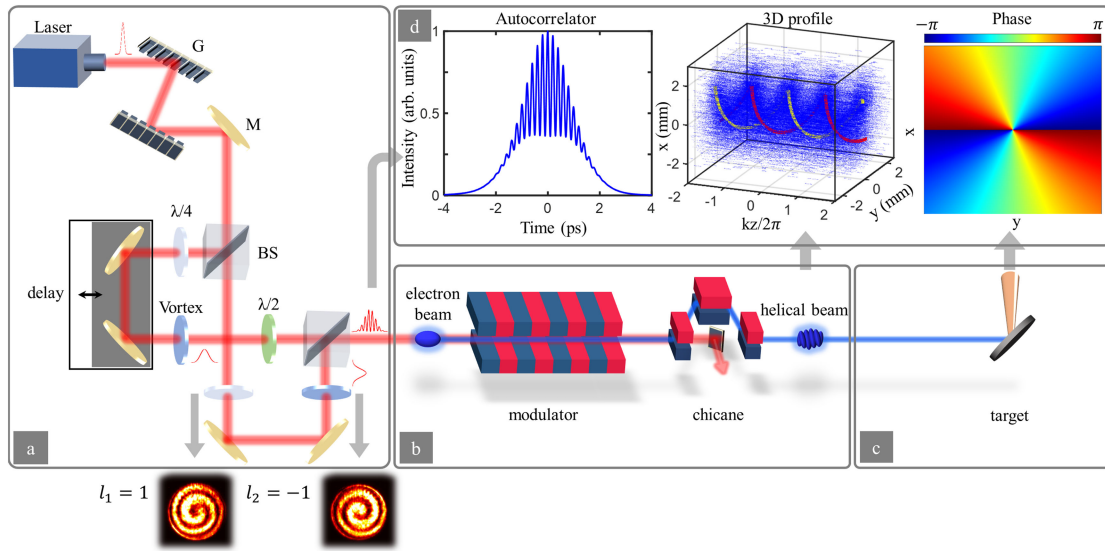
Fig. 1. Schematic layout for the (a) optical module with the measurement of the vortex wavefront, (b) modulation module, and (c) radiation module. In (d), there are measurement of autocorrelator signal (left), simulation of helical microbunching structure (middle) and wavefront phase of THz emission from radiator (right).

First of all, higher harmonics of the undulator radiation were observed to possess OAM, corresponding to the Laguerre–Gaussian (LG) modes, when the undulator is operated in a circular polarization scheme [28]. However, the harmonics have weak power and an additional filter is required to block the dominated fundamental. Utilizing the longitudinally microbunched electron beam can effectively improve the brightness of harmonic vortices emission [29]. Furthermore, a more general and novel method is proposed to generate vortex beams, while the notion is to obtain a helically microbunched electron beam based on laser-beam interaction. This can be accomplished by two approaches. The first one exploits the seed laser to excite the harmonics of the helical undulator to couple the azimuthal mode to the electron [30]. The second one directly replaces the seed by a vortex laser to modulate the electron on the fundamental of the undulator [31]. Then, both of them need a dispersion section to convert the energy modulation to a helical microbunching. Whereby this helically microbunched electron beam, a variety of radiation methods can be used to emit vortex beams, such as, superradiation, transition radiation and undulator radiation. Already, some schemes have been proposed to generate extreme-ultraviolet or soft x-ray vortex combined with some up-frequency setups [31], [32]. Most recently, a straightforward method is also presented to generate intense OAM beams from an X-ray free-electron laser oscillator [33].

For the radiation source with wavelength in the THz band, based on laser-electron interaction technology, many schemes are proposed to control the properties of THz radiations [34], [35]. As a matter of fact, it has already been experimentally applied to generate narrow-band THz radiation in electron accelerators [36]–[39]. A proposal for THz vortex radiation was born from the aforementioned first approach developed to describe the twice coupling and evolution of higher-order optical mode structures and e-beam in two modulators [40]. However, due to the harmonic resonance of the seed lasers,

the coupling efficiency between the higher-order optical mode and electron is less compared to that of the fundamental one. Especially, to reach a larger topological charge, a laser with higher energy is required to maintain the modulation effect for the helically microbunched electron beam. This limits the tunability of quantum number. Two modulators with opposite circular polarization are imperatively needed in it, which isn't conducive to experimentally practice.

In this paper, we present the possibility of controlling the helical mode number of electron beam for getting THz vortex radiation with tunable quantum number, and the general schematic is shown in Fig. 1. The electron beam and the laser pulse with longitudinal and azimuthal modulation fully interact on the fundamental of the undulator (called modulator for few period number). This shaped laser pulse is obtained by optical beating of two branches of pulses with different quantum numbers, and it finally makes the electron beam forming a sub-mm spiral microstructure in space after a dispersion section. This kind of electron beam can be regarded as a medium of frequency and mode converter, which can generate intense THz radiation in the downstream radiator and transfer the transverse mode of the seed laser into the THz radiation pulse. The topological charge of THz radiation is directly determined by the optical laser, and the adjustment range of the quantum number is increased by the fact of that two branches of pulses with different quantum numbers are utilized. Moreover, since only one modulator and vortex seed laser are required, it is suitable and compatible for existing accelerator devices with laser-electron modulation.

This article is structured as follows. Section II demonstrates the optical system to generate the targeted laser beam. Then, in Section III, it's explained in both theory and simulation that the generation of helically microbunched electron beam by laser-electron interaction. The tunability of the helical mode numbers on modulated electron beam is discussed in Section IV.

The ultimate purpose of generating helically microbunched electron beams is to obtain THz vortex beams. As discussed in Section V, narrowband THz vortex beams with different polarization states can be obtained by transiting radiation and undulator radiation. Lastly, summary is given in Section VI.

II. EXPERIMENTAL DEMONSTRATION OF OPTICAL SYSTEM

Fig. 1(a) shows the optical system to support the required seed laser. An ultrashort fs laser pulse is firstly stretched to ps scale by a grating pair (G). Then a Michelson interferometer system is used to accomplish the chirped-pulse beating process, where the pulse is split equivalently by a beam splitter (BS) and recombined with a variable time delay. Different from the routine chirped-pulse beating [41], the $\lambda/2$, $\lambda/4$ and vortex waveplates are inserted in the light path before beating. The $\lambda/4$ waveplates can transfer the linear polarization to circular polarization so that the vortex waveplates can convert the plane wavefront into vortex wavefront, and the chirality is determined by the polarization state of the input pulse. The output vortex pulses with different chirality have opposite polarizations. A $\lambda/2$ waveplate is applied to make these two pulses having the same circular polarization so that they can beat to form an intensity modulation.

A simplified theoretical analysis will be given to describe the entire optical process. The electric field of initial transform-limited Gaussian pulse with linear polarization is given by,

$$\mathbf{E}_{in}(t,r) = \mathcal{E}exp(-r^2/w_0^2 - t^2/\sigma_0^2 + i\omega_0 t)\hat{\mathbf{e}}_\perp, \quad (1)$$

with the longitudinal time coordinate t and radial coordinate r. $\hat{\mathbf{e}}_\perp$ is the unit vector representing the direction of linear polarization, $\mathcal{E}$ is the amplitude, σ_0 is the pulse width, w_0 is the waist size and ω_0 is the central angular frequency. Firstly, the wideband pulse is stretched in time by the diffraction grating pair (G) up to second-order dispersion, yielding a linearly chirped pulse as,

$$\mathbf{E}_{out}(t,r) = \mathcal{E}\sqrt{\frac{\sigma_0}{\sigma_n}}exp\left[-r^2/w_0^2 - t^2/\sigma_n^2 + i(\omega_0 t + \alpha t^2)\right]\hat{\mathbf{e}}_\perp,$$
$$(2)$$

where σ_n is the stretched width of output pulse and $\alpha \simeq 1/\sigma_0\sigma_n$ is the chirp parameter. Then, two identical pulses are obtained after the beam splitter (BS), $\mathbf{E}_1(t,r) = \mathbf{E}_2(t,r) = \frac{1}{2}\mathbf{E}_{out}(t,r)$. Under the effect of $\lambda/4$ waveplates, the polarization of the two pulses transfers to opposite circular polarization. Hence, the opposite chirality is obtained by vortex waveplates. To ensure the beating process, the $\lambda/2$ waveplate is applied to align the polarization states of the two beams. Therefore, two pulses with opposite handedness but same circular polarization are generated before beating, and for simplicity the fields are approximated as,

$$\mathbf{E}_1(t,r,\phi) = \mathcal{E}_1\left(\frac{\sqrt{2}r}{w_0}\right)^{|l_1|} e^{-r^2/w_0^2 - t^2/\sigma_n^2} e^{i(\omega_0 t + \alpha t^2 + l_1\phi)}\hat{\mathbf{e}}_c,$$

$$\mathbf{E}_2(t,r,\phi) = \mathcal{E}_2\left(\frac{\sqrt{2}r}{w_0}\right)^{|l_2|} e^{-r^2/w_0^2 - t^2/\sigma_n^2} e^{i(\omega_0 t + \alpha t^2 + l_2\phi)}\hat{\mathbf{e}}_c,$$
$$(3)$$

where $\hat{\mathbf{e}}_c = (\hat{\mathbf{e}}_x \pm \hat{\mathbf{e}}_y)/\sqrt{2}$ correspond to circular polarization, $\mathcal{E}_1$, $\mathcal{E}_2$ are field amplitude coefficients. The transverse modes are excited in azimuthal coordinate ϕ. l_1 and l_2 are the topological charges of the laser beams from two vortex waveplates respectively. They are controlled by changing the vortex waveplates.

Finally, with a time delay τ, these two pulses recombine and the output optical intensity from Michelson interferometer is expressed as $I_{total} = \frac{1}{2}|\mathbf{E}_1(t + \frac{\tau}{2}, r, \phi) + \mathbf{E}_2(t - \frac{\tau}{2}, r, \phi)|^2 = I_+ + I_- + I_{cross}$. The pivotal cross term is given by,

$$I_{cross}(t,r,\phi) = \mathcal{E}_1\mathcal{E}_2\left(\frac{\sqrt{2}r}{w_0}\right)^{|l_1|+|l_2|}$$
$$\times exp\left(-\frac{2r^2}{w_0^2} - \frac{2t^2}{\sigma_n^2} - \frac{\tau^2}{2\sigma_n^2}\right)$$
$$\times \cos\left[2\alpha\tau t + (l_1 - l_2)\phi + \omega_0\tau\right]. \quad (4)$$

It can be seen that the last term has not only a modulation in longitudinal time coordinate t, but also an azimuth-dependence modulation in transverse coordinate ϕ. The first two terms $I_\pm$ only add a Gaussian envelope and have no effect on the modulation frequency and helical mode. According to (4), the beating angular frequency ω_m and the mode number l_m of the intensity modulation can be written as,

$$\omega_m = 2\alpha\tau,$$
$$l_m = l_1 - l_2. \quad (5)$$

The modulation frequency is directly determined by the dispersion medium and the time delay, and the azimuthal mode number is determined by the topological charge of the two vortex pulses.

The optical system has been demonstrated as shown in Fig. 1. A Ti:Sapphire femtosecond laser source centered at 800 nm wavelength provides a linearly polarized pulse with 46 fs pulse width. After passing the grating pair (grating line: 1200 mm^{-1}; incident angle: 60°; grating pair distance: 3 cm), the pulse is stretched and chirped, and then it can be converted to vortex beam in the following vortex waveplate. When the two pulses with different circular polarizations traverse the vortex wave-plates respectively, the vortex wavefronts with different handedness can be obtained. They are measured by the interference with Gaussian pulses which have spherical wavefronts, and the results are shown in Fig. 2. The interference images in Fig. 2(a) and (b) have distinct opposite rotation directions, which display the opposite chirality of $l_1 = 1$ and $l_2 = -1$ respectively. With such a configuration, a chirp parameter of $\alpha = 15.87$ ps^{-2} is introduced in the pulse. As shown in Fig. 1(d), the autocorrelator records an example of the beating pulse shape with $\omega_m/2\pi = 5$ THz when time delay is set at $\tau = 1.1$ ps. Further, through shifting the delay τ, the modulation frequency can be changed correspondingly. Fig. 3 shows the scanning spectrum of autocorrelator signals with different time delay τ. Therefore, the modulation frequency ω_m can be adjusted by optical delay line, and the mode number l_m can also be directly tuned by changing vortex waveplates, as shown in Fig. 1(a).
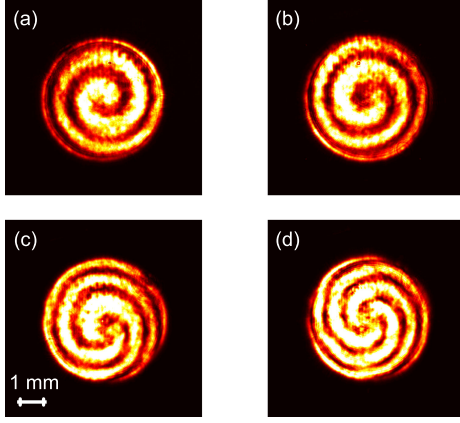
Fig. 2. Interference patterns of vortex beams with different topological charges of (a) −1, (b) 1, (c) 2, and (d) 3.
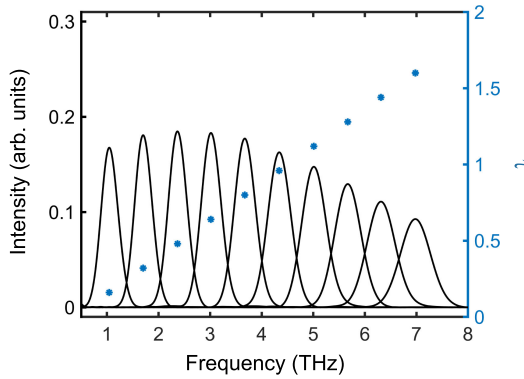

Fig. 3. Spectrum of the autocorrelator signal with different time delay τ.

III. GENERATION OF HELICAL MODULATION IN ELECTRON BEAM: THEORY AND SIMULATION

As shown in Fig. 1(b), the electron beam modulation system consisted of a modulator and a dispersion section (i. e., chicane) is applied to impose a spiral modulation on a relativistic electron beam. The modulator resonates at the laser wavelength for laser-electron interaction. The beating laser pulse enters the modulator together with electron beam, and the magnetic field of modulator introduces a transverse momentum to electron so that the beam can exchange energy with the laser field. Corresponding to the spiral distribution of the laser intensity, the electron beam obtains a helical energy modulation. Then, electrons with different energies go through orbits with different lengths, leading to an electron beam with corkscrew geometry. Detailed theory discussions and simulation results are given in following.

The laser-electron interaction in modulator can be analytically described in a linear equation. The initial distribution of an axisymmetric electron beam is,

$$f_i(p, r) = \frac{N_0}{\sqrt{2\pi}} f_0(r) e^{-\frac{p^2}{2}}, \quad (6)$$

where N_0 is the number of electrons per unit length, $p = (\gamma - \gamma_0)/\sigma_\gamma$ is the dimensionless energy deviation normalized to energy spread σ_γ and γ_0 is the average energy. $f_0(r) = \frac{1}{\sigma_r^2} e^{-r^2/2\sigma_r^2}$ is the radial distribution with a transverse size σ_r.

In a modulator with a bandwidth larger than that of the seed laser pulse, the transverse components of electron velocity can effectively change energy with the field of electromagnetic wave as $d\gamma/dz = -e\mathbf{v}_\perp \cdot (\mathbf{E}_1 + \mathbf{E}_2)$, where $\mathbf{v}_\perp$ is the transverse velocity of electron in modulator. With a short interaction length in modulator, the energy changes of the relativistic electron at resonance can be linearized as,

$$p' = p + \bar{A}_1(r) \cos[\omega_0(t + \tau/2) + \alpha(t + \tau/2)^2 + l_1\phi]$$
$$+ \bar{A}_2(r) \cos[\omega_0(t - \tau/2) + \alpha(t - \tau/2)^2 + l_2\phi], \quad (7)$$

where $\bar{A}_i(r) = A_i(\sqrt{2}r/w_0)^{|l_i|} exp(-r^2/w_0^2)$ are the radial modulation amplitudes. For simplicity sake, we neglect the slow varying Gaussian envelope of the laser pulse, which has no essential influence on the analysis. Then, the chicane with a momentum compaction factor R_{56} changes the longitudinal position as $t' = t + R_{56}p'\frac{\sigma_\gamma}{c\gamma_0}$, where $t \approx z/c$ and c is the light speed. Finally, the distribution function becomes,

$$f_f(p',' t,' r, \phi) = \frac{N_0}{\sqrt{2\pi}} f_0(r) exp\bigg\{ -\frac{1}{2}\bigg[p' - \bar{A}_1(r)$$
$$\times \cos\bigg(\omega_0\bigg(t' - Kp' + \frac{\tau}{2}\bigg) + \alpha\bigg(t' - Kp' + \frac{\tau}{2}\bigg)^2 + l_1\phi\bigg) - \bar{A}_2(r)$$
$$\times \cos\bigg(\omega_0\bigg(t' - Kp' - \frac{\tau}{2}\bigg) + \alpha\bigg(t' - Kp' - \frac{\tau}{2}\bigg)^2 + l_2\phi\bigg)\bigg]^2\bigg\}, \quad (8)$$

with $K = R_{56}\sigma_\gamma/c\gamma_0$.

We give the helical bunching factor (The radiation intensity is proportional to its square) to investigate the Fourier characteristics at frequency ω and helical mode l of such a distribution:

$$b(\omega, l) = \frac{1}{N_0} \left| \langle e^{-i\omega t'} e^{-il\phi} N(t,' \phi) \rangle \right|, \quad (9)$$

where $N(t,' \phi) = \int \int_{-\infty}^{+\infty} dr dp' f_f(p,' t,' r, \phi)$ is the beam density in both longitudinal and azimuthal coordinates, the brackets denote averaging over the coordinates t' and ϕ, and ω, l are the Fourier components corresponding to t' and ϕ respectively. The helical bunching factor is not zero only if

$$\omega = n\omega_m,$$
$$l = nl_m, \quad (10)$$

where n donates the harmonics. It states that the modulated electron gets multiple Fourier components at different frequencies and azimuthal modes. After some mathematical manipulations the helical bunching factor can be written as,

$$b_n = \bigg| e^{-\frac{1}{2}n^2\omega_m^2 K^2}$$
$$\times \int J_n[-n\omega_m K\bar{A}_1(r)] J_{-n}[-n\omega_m K\bar{A}_2(r)] f_0(r) r dr \bigg|, \quad (11)$$

where $J_{\pm n}$ are Bessel functions.

As an example, we consider the fundamental bunching factor of $n = 1$. The modulation frequency and mode number of the above demonstrated output pulse are $\omega_m/2\pi = 5$ THz and $l_m = 2$. With the pulse size $w_0/\sigma_r = 2$, we give the relation between fundamental bunching factor b_1 and modulation coefficients A_i in Fig. 4, where the bunching factor is maximized through
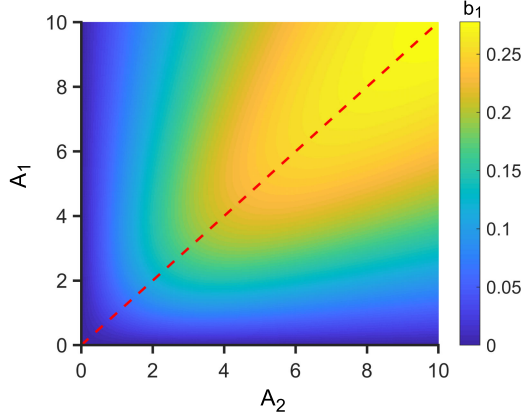
Fig. 4. Helical bunching factor VS modulation amplitude coefficients. The red dotted line corresponds to the case of $A_1 = A_2$.

TABLE I
PARAMETERS OF ELECTRON BEAM AND MODULATOR

Electron beam	Value
Beam energy	120 MeV
Energy spread	12 keV
Beam size (rms)	1 mm
Normalized emittance (rms)	2 mm·mrad
Beam charge	1 nC
Modulator	Value
K	0.8
Period length	3 cm
Period number	5

Fig. 5. The phase space of electron beam at the exit of chicane (a) the helical bunching factor VS momentum compaction R_{56} (b) and its spectrum for different harmonics (c).

Fig. 6. (a) Radial intensity profiles of laser with different topological charges. (b) Helical bunching factor VS laser pulse waist for different l_1 and l_2, where $l_1 = -l_2$.

scanning the momentum compaction factor R_{56}, according to Eq. (8). One can see that the helical bunching factor increases with the modulation amplitudes and tends to saturation when A_i are larger than 5. When A_1 and A_2 are equal to each other (showed in Fig. 4 by red dotted line), the bunching factor b_1 can reach a optimal value, and it corresponds to the case of the same absolute values of topological charges, $|l_1| = |l_2|$.

Further, we simulate the modulation process numerically. Considering the whole modulation process can be described linearly, we neglect the slippage effect due to the few period number of modulator and the space charge effect for a relativistic energy. The laser pulse described in last section with considering longitudinal Gaussian envelope is used as a seed to modulate the beam whose parameters are given in Table I. The modulation coefficients are set at $A_1 = A_2 = 5$. The longitudinal phase space of the electron beam at the exit of chicane is shown in Fig. 5(a). It can be seen that there is an envelope at THz scale. The spatial distribution of the helically microbunched electron beam is shown in Fig. 1(d), and the twisted geometry indicates the helical mode number of $l_m = 2$.

The harmonics of different n are investigated through viewing the changes under different R_{56}. As can be seen in Fig. 5(b), there are obvious frequency components up to $n = 3$ in the helical bunching factors, but they reach maximum at different R_{56}. When b_1 is maximized at $R_{56} = 50$ mm, one can see a considerable second harmonic $b_2 = 0.05$ in the spectrum of Fig. 5(c), and the third harmonic is negligible due to a inapposite dispersion effect.
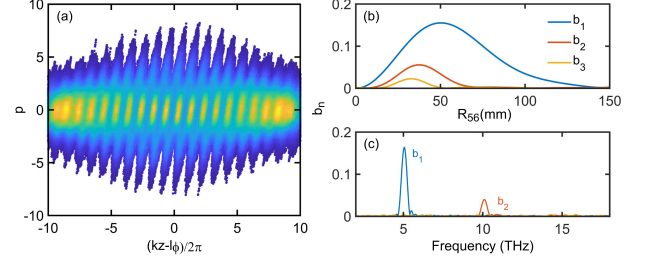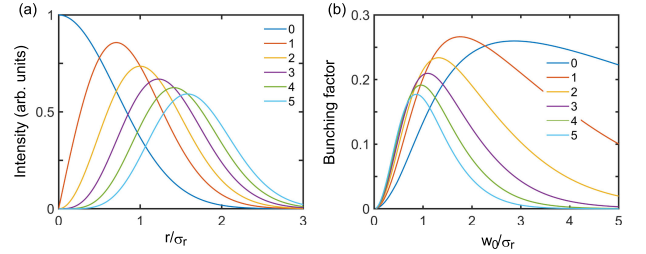
IV. TUNABILITY OF THE HELICAL MODE NUMBERS ON ELECTRON BEAM

The tunability of helical mode number on the electron beam is a more interesting topic, which can directly determine the quantum numbers of the radiation from helically microbunched electron beam. According to (3), the simplest way in our proposed scheme is to change the configuration of vortex waveplates to vary the topological charge l_1 and l_2 of the laser pulses. In principle, one can generate electron beam with arbitrary helical mode numbers through using optical vortex laser with corresponding topological charges. However, considering the complexity of larger helical mode, we need to evaluate the performance with increasing mode numbers.

With a fixed pulse energy (a 10 mJ pulse can lead to a peak modulation amplitudes $A_1 = A_2 = 5$ while $l_1 = l_2 = 0$), the radial intensity profiles with different topological charges are show in Fig. 6(a). The maximum intensity decreases and the position of peak intensity ring shifts outward as the increasing of topological charges. It can be foreseen that a seed laser with larger quantum number leads to a smaller modulation amplitude on the core of electron beam. Then, through scanning the waist size of laser pulse according to (8), it is shown in Fig. 6(b) that the helical bunching factor can be maximized with specific waists for different mode numbers $l_1 = -l_2 = 1, 2, 3, 4, 5$. As expected, the optimal ratio of waist and bunch size is decreasing with the increasing of topological charges so that more electrons can interact with the peak filed of laser. So it's necessary to modify the radial size of laser to enhance the helical bunching factors for larger mode numbers.

A bubble diagram is given in Fig. 7(a) to show the helical bunching factor with variety combinations of l_1 and l_2. It can be
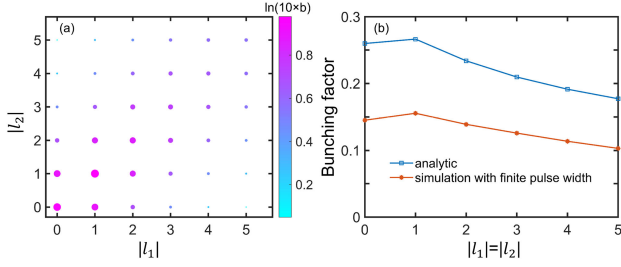
Fig. 7. (a) The helical bunching factor with combinations of different topological charges. (b) The comparison of analytic and simulation results.
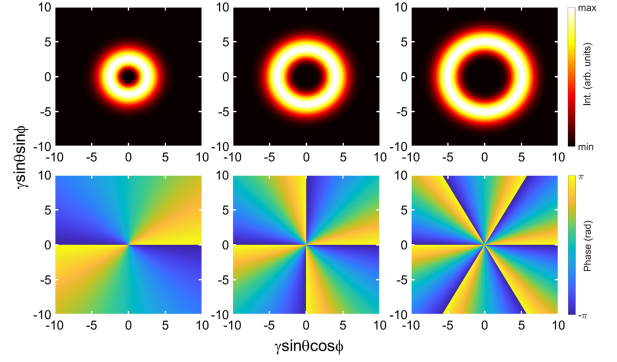

Fig. 8. Transverse profiles of transition radiation intensity and wave-front phase at fundamental $n = 1$. Left: $l = 2(l_1 = 1, l_2 = -1)$. Middle: $l = 4(l_1 = 2, l_2 = -2)$. Right: $l = 6(l_1 = 3, l_2 = -3)$.

found that a larger bunching factor concentrates on smaller and equal topological charges of $|l_1|$ and $|l_2|$. With a large difference between $|l_1|$ and $|l_2|$, the two optical vortex beams can't overlap well transversely. Besides, the above theory neglects the laser pulse width, so we give the simulation results in Fig. 7(b) together with the analytic cases. They keep a similar variation tendency, and the simulation results are smaller due to the consideration of finite pulse width. However, the value of the helical bunching factor can be larger than 0.1 up to $|l_1| = |l_2| = 5$.

V. RADIATION FROM THE HELICALLY MICROBUNCHED ELECTRON BEAM

A. Transition Radiation

A charged particle crossing the boundary between two different media generates transition radiation (TR) of radial polarization. It can be used not only to obtain the optical beam carrying orbital angular momentum from a helically microbunched electron beam, but also to diagnose the complex helical microbunching structures of electron beam. The obtained vortex pulse maintains the characteristic of radial polarization. With a constant velocity in vacuum, a single electron is assumed to strike a transversely infinite perfect conductor, and the spectral radiation energy measured in a region far beyond the formation zone is,

$$\frac{d^2U_0}{dkd\Omega} = \frac{e^2}{4\pi^3\varepsilon_0}\frac{\beta^2\sin^2\theta}{(1-\beta^2\cos^2\theta)^2}, \quad (12)$$

where $k = \omega/c$ is the emission wave number and $d\Omega = \sin\theta d\theta d\phi$ is the solid angle with the forward opening angel θ.

TR can be enhanced coherently at frequencies for which the emission from bunched electrons are in phase, so the coherent transition radiation (CTR) spectral energy from a beam is given by,

$$\frac{d^2U}{dkd\Omega} = N_e^2 F(k)\frac{d^2U_0}{dkd\Omega}, \quad (13)$$

where N_e is the number of electrons, $F(k)$ is the form factor of electron beam and the divergence of the beam is ignorable compared with the small emission angle. Different from the normal one-dimensional longitudinal modulation [42], a detailed description of the form factor is needed to expound the complex higher-order bunching structures. For emission at wavelengths much shorter than the finite bunch length, the distribution of beam can be expanded into a series orthogonal basis functions so that the form factor can associate with the helical bunching factor

mentioned above at different harmonics n and helical modes l as [43],

$$\sqrt{F(k)} = \frac{1}{2}\sum_{n=1}^{\infty}\sum_{l=-\infty}^{\infty} b_n \frac{1}{(|l|/2)!}\left(\frac{k\sigma_r\sin\theta}{\sqrt{2}}\right)^{|l|}$$

$$\times exp\left\{-\frac{\sigma_z^2}{2}(nk_m - k\cos\theta)^2 - \frac{\sigma_r^2}{2}(k\sin\theta)^2 + il(\phi - \pi/2)\right\}, \quad (14)$$

where we only consider the dominated fundamental radial mode, $k_m = \omega_m/c$ is the wave number of modulated electron beam, and σ_z is the finite bunch length.

Final, the radiation spectrum of beam is described as,

$$\frac{d^2U}{dkd\Omega} = \frac{N_e^2 e^2}{16\pi^3\varepsilon_0}\frac{\sin^2\theta}{(1-\beta^2\cos^2\theta)^2} \times \left|\sqrt{F(k)}\right|^2. \quad (15)$$

One can see that the radiation spectrum is peaked around $k \simeq nk_m$ for small forward angle, and there is an azimuthal phase dependence of $exp(il\phi)$, which indicates the CTR from helical electron beam carries nonzero OAM. Using aforementioned parameters of helically microbunched electron beam, we consider CTRs with several cases of different topological charges. According to (15), the transverse distributions of radiation intensity and phase at fundamental frequencies are illustrated in Fig. 8. The doughnut-shaped intensity profiles expand outward with the increasing of topological charges, as expected.

Using above electron parameters, an integration of (15) around 5 THz frequency in 1% bandwidth gives the angular energy distribution as shown in Fig. 9, while the beam length is $\sigma_z = 1$ mm and beam charge is set at 1 nC. It can be found that the fundamental $n = 1$ is dominant and the emission intensity decreases with the increasing of the helical mode number. Higher electron beam charge and energy can produce a higher radiation pulse energy.

B. Undulator Radiation

Undulator radiation is also an excellent choice to extract helical mode from electron beam to THz pulse. Different from the radial polarization of transition radiation, the undulator radiation has the characteristic of variable polarization from linear to circular polarization when a helical undulator is applied. So it's worth mentioning that using different methods for radiation
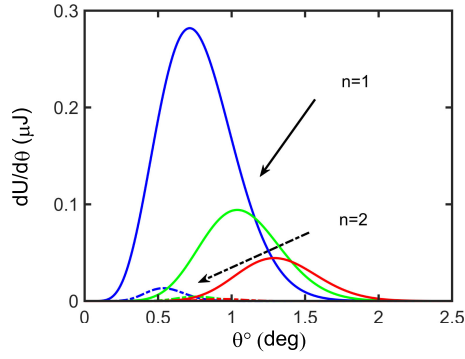
Fig. 9. Angular profiles of the radiation energy for fundamental $n = 1$ (solid line) and harmonic $n = 2$ (dotted dash line) with $l_1 = 1, l_2 = -1$ (blue); $l_1 = 2, l_2 = -2$ (green); $l_1 = 3, l_2 = -3$ (red).
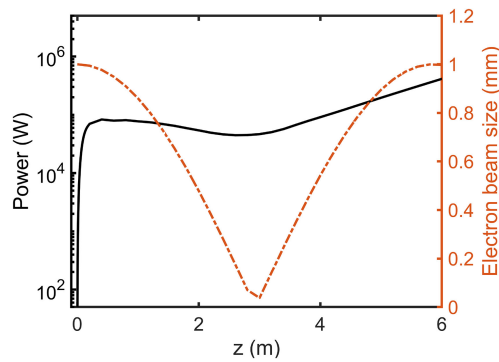

Fig. 10. The radiation power evolution along the undulator together with the variation of the electron beam size.
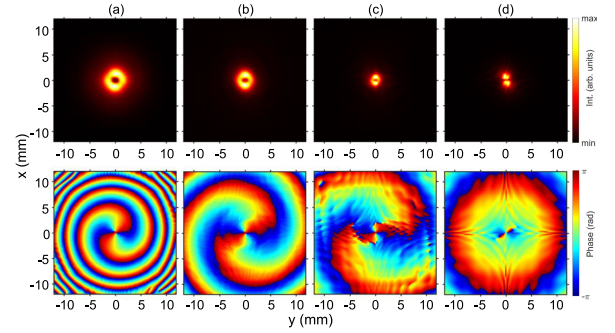

Fig. 11. Transverse intensity profiles of undulator radiation and wave-front phase at (a) $z = 0.4$ m, (b) $z = 1.2$ m, (c) $z = 2$ m, and (d) $z = 4$ m.

we can control the spin angular momentum of the THz pulse together with the orbital angular momentum, which can be applied to spectroscopy of magnetic excitations.

Using the helically microbunched electron beam at the mode of $l = 2$ ($l_1 = 1, l_2 = -1$), the simulation is performed by the code Genesis [44]. The power along the undulator is shown in Fig. 10 for a circular radiator, and the undulator period number is $n = 30$ with the undulator parameter $K = 8$ and the period length $\lambda_u = 0.2$ m. With an initial helical bunching factor over 0.15 which is larger than the shot noise, the radiation power is quickly amplified to 0.1 MW at the entrance of the radiator. Then, after a long lethargy, the amplification restarts again. To explore such the gain process and the field mode, the transverse intensity and phase front at different position of undulator are shown in Fig. 11. One can find that the OAM mode of $l = 2$ is dominant with a hollow distribution and a helical wave-front in the first several periods (see Fig. 11(a), (b)). Then, with the increase of the undulator length, the helical phase mode is suppressed, leading to a distortion (Fig. 11(c)). Final, the Gaussian mode dominates the optical field (Fig. 11(d)). In this regard, the rapid mode distortion mainly stems from the variation of the electron beam size. The evaluation of the electron beam size is shown in Fig. 10. The natural focusing in undulator sharply reduces the beam size with a period of $\lambda_\beta = \lambda_u \gamma / K = 5.9$ m. It affects the complex spiral structure of the helically microbunched electron beam so that the transverse mode can't maintain in a long distance. The simulations are also performed for a planar regime.

Its radiation power can only reach 0.05 MW at $z = 0.6$ m. It seems that the natural focusing of a single direction in the planar undulator has a greater effect on the helical structure of the electron beam.

In practical applications, to ensure the purity of the vortex beam, one can use a short undulator with less period number. The radiation pulse can reach saturation at the exit of the undulator with the vortex mode dominant. The radiation power can be directly improved by increasing the electron beam bunching factor or increasing the beam charge. Moreover, through increasing the oscillation period λ_β, the helical structure of the electron beam can be maintained longer so that one can increase the radiation power and energy by using a longer undulator. Further detailed works are required to be perform on the undulator radiation.

VI. Summary

We have identified a novel scheme of generating helical microbunching structure in relativistic electron beam for the generation of THz vortex. An optical system is demonstrated to support a complex azimuthal-dependent lasers by dual-vortex beating. This shaped seed laser modulates electron beam in a modulator and emerges a helical microbunching in the beam after a dispersion section. The THz emission with orbital angular momentum can be generated from such an electron beam. The complex helical mode is directly inherited from lasers, which makes it easy to tune the helical mode number and also the final topological charges of THz radiation. Besides, the THz frequency can also be tuned continuously by adjusting the optical delay line in the beating optics. Together with the control of orbital angular momentum, different radiation methods are studied to control the spin angular momentum of the THz vortex. The radial polarization can be obtain from transition radiation and the undulator can supply a variable polarization from linear to circular polarization. It gives the possibility of comprehensive control on the angular momentum of THz radiation to open up more researches in THz science.

References

[1] Y. Shen *et al.*, "Optical vortices 30 years on: OAM manipulation from topological charge to multiple singularities," *Light: Sci. Appl.*, vol. 8, no. 1, 2019, Art. no. 90.

[2] J. Wang *et al.*, "Terabit free-space data transmission employing orbital angular momentum multiplexing," *Nature Photon.*, vol. 6, no. 7, pp. 488–496, 2012.

[3] I. Heller *et al.*, "Sted nanoscopy combined with optical tweezers reveals protein dynamics on densely covered dna," *Nature Methods*, vol. 10, no. 9, pp. 910–916, 2013.

[4] M. Padgett and R. Bowman, "Tweezers with a twist," *Nature Photon.*, vol. 5, no. 6, pp. 343–348, 2011.

[5] M. Van Veenendaal and I. McNulty, "Prediction of strong dichroism induced by x rays carrying orbital momentum," *Phys. Rev. Lett.*, vol. 98, no. 15, 2007, Art. no. 157401.

[6] A. Picón, J. Mompart, J. De Vázquez Aldana, L. Plja, G. Calvo, and L. Roso, "Photoionization with orbital angular momentum beams," *Opt. Exp.*, vol. 18, no. 4, pp. 3660–3671, 2010.

[7] A. Rury, "Examining resonant inelastic spontaneous scattering of classical Laguerre-Gauss beams from molecules," *Phys. Rev. A - Atomic, Mol., Opt. Phys.*, vol. 87, no. 4, 2013, Art. no. 043408.

[8] T. Kampfrath, K. Tanaka, and K. Nelson, "Resonant and nonresonant control over matter and light by intense terahertz transients," *Nature Photon.*, vol. 7, no. 9, pp. 680–690, 2013.

[9] A. Sirenko, P. Marsik, C. Bernhard, T. Stanislavchuk, V. Kiryukhin, and S.-W. Cheong, "Terahertz vortex beam as a spectroscopic probe of magnetic excitations," *Phys. Rev. Lett.*, vol. 122, no. 23, 2019, Art. no. 237401.

[10] A. Sirenko *et al.*, "Total angular momentum dichroism of the terahertz vortex beams at the antiferromagnetic resonances," *Phys. Rev. Lett.*, vol. 126, no. 15, 2021, Art. no. 157401.

[11] X. Wang, Z. Nie, Y. Liang, J. Wang, T. Li, and B. Jia, "Recent advances on optical vortex generation," *Nanophotonics*, vol. 7, no. 9, pp. 1533–1556, 2018.

[12] L. Zhu and J. Wang, "A review of multiple optical vortices generation: Methods and applications," *Front. Optoelectron.*, vol. 12, no. 1, pp. 52–68, 2019.

[13] T. Omatsu, K. Miyamoto, and A. Lee, "Wavelength-versatile optical vortex lasers," *J. Opt.*, vol. 19, no. 12, 2017, Art. no. 123002.

[14] X. Wang *et al.*, "Longitudinal field characterization of converging terahertz vortices with linear and circular polarizations," *Opt. Exp.*, vol. 24, no. 7, pp. 7178–7190, 2016.

[15] B. Knyazev, Y. Choporova, M. Mitkov, V. Pavelyev, and B. Volodkin, "Generation of terahertz surface plasmon polaritons using nondiffractive bessel beams with orbital angular momentum," *Phys. Rev. Lett.*, vol. 115, no. 16, 2015, Art. no. 163901.

[16] J. He *et al.*, "Generation and evolution of the terahertz vortex beam," *Opt. Exp.*, vol. 21, no. 17, pp. 20230–20239, 2013.

[17] S. Ge *et al.*, "Terahertz vortex beam generator based on a photopatterned large birefringence liquid crystal," *Opt. Exp.*, vol. 25, no. 11, pp. 12349–12356, 2017.

[18] S.-J. Ge *et al.*, "Generating, separating and polarizing terahertz vortex beams via liquid crystals with gradient-rotation directors," *Crystals*, vol. 7, no. 10, 2017, Art. no. 314.

[19] Z.-X. Shen *et al.*, "Planar terahertz photonics mediated by liquid crystal polymers," *Adv. Opt. Mater.*, vol. 8, no. 7, 2020, Art. no. 1902124.

[20] K. Miyamoto, K. Suizu, T. Akiba, and T. Omatsu, "Direct observation of the topological charge of a terahertz vortex beam generated by a tsurupica spiral phase plate," *Appl. Phys. Lett.*, vol. 104, no. 26, 2014, Art. no. 261104.

[21] K. Miyamoto *et al.*, "Highly intense monocycle terahertz vortex generation by utilizing a tsurupica spiral phase plate," *Sci. Rep.*, vol. 6, no. 1, 2016, Art. no. 38880.

[22] K. Miyamoto *et al.*, "Generation of high-quality terahertz OAM mode based on soft-aperture difference frequency generation," *Opt. Exp.*, vol. 27, no. 22, pp. 31840–31849, 2019.

[23] Q. Lin *et al.*, "Generation of terahertz vortex pulses without any need of manipulation in the terahertz region," *Opt. Lett.*, vol. 44, no. 4, pp. 887–890, 2019.

[24] H. Wang, Y. Bai, E. Wu, Z. Wang, P. Liu, and C. Liu, "Terahertz necklace beams generated from two-color vortex-laser-induced air plasma," *Phys. Rev. A*, vol. 98, no. 1, 2018, Art. no. 013857.

[25] M. Ivanov, I. Thiele, L. Bergé, S. Skupin, D. Buožius, and V. Vaičaitis, "Intensity modulated terahertz vortex wave generation in air plasma by two-color femtosecond laser pulses," *Opt. Lett.*, vol. 44, no. 15, pp. 3889–3892, 2019.

[26] S. Sasaki, I. McNulty, and R. Dejus, "Undulator radiation carrying spin and orbital angular momentum," *Nucl. Instruments Methods Phys. Res., Sect. A: Accelerators, Spectrometers, Detectors Assoc. Equip.*, vol. 582, no. 1, pp. 43–46, 2007.

[27] S. Sasaki and I. McNulty, "Proposal for generating brilliant X-ray beams carrying orbital angular momentum," *Phys. Rev. Lett.*, vol. 100, no. 12, 2008, Art. no. 124801.

[28] J. Bahrdt, K. Holldack, P. Kuske, R. Müller, M. Scheer, and P. Schmid, "First observation of photons carrying orbital angular momentum in undulator radiation," *Phys. Rev. Lett.*, vol. 111, no. 3, 2013, Art. no. 034801.

[29] E. Hemsing, M. Dunning, C. Hast, T. Raubenheimer, and D. Xiang, "First characterization of coherent optical vortices from harmonic undulator radiation," *Phys. Rev. Lett.*, vol. 113, no. 3, 2014, Art. no. 134803.

[30] E. Hemsing *et al.*, "Coherent optical vortices from relativistic electron beams," *Nature Phys.*, vol. 9, no. 9, pp. 549–553, 2013.

[31] E. Hemsing and A. Marinelli, "Echo-enabled X-ray vortex generation," *Phys. Rev. Lett.*, vol. 109, no. 22, 2012, Art. no. 224801.

[32] P. Ribič, D. Gauthier, and G. De Ninno, "Generation of coherent extreme-ultraviolet radiation carrying orbital angular momentum," *Phys. Rev. Lett.*, vol. 112, no. 20, 2014, Art. no. 203602.

[33] N. Huang and H. Deng, "Generating X-rays with orbital angular momentum in a free-electron laser oscillator," *Optica*, vol. 8, no. 7, pp. 1020–1023, 2021.

[34] D. Xiang and G. Stupakov, "Enhanced tunable narrow-band thz emission from laser-modulated electron beams," *Phys. Rev. ST Accel. Beams*, vol. 12, no. 8, 2009, Art. no. 080701.

[35] H. Zhang *et al.*, "Chirp control of tunable terahertz synchrotron radiation," *Opt. Lett.*, vol. 45, no. 17, pp. 4674–4677, 2020.

[36] S. Bielawski *et al.*, "Tunable narrowband terahertz emission from mastered laser-electron beam interaction," *Nature Phys.*, vol. 4, no. 5, pp. 390–393, 2008.

[37] P. Ungelenk *et al.*, "Continuously tunable narrowband pulses in the thz gap from laser-modulated electron bunches in a storage ring," *Phys. Rev. Accelerators Beams*, vol. 20, no. 2, 2017, Art. no. 020706.

[38] Y. Shen, X. Yang, G. L. Carr, Y. Hidaka, J. B. Murphy, and X. Wang, "Tunable few-cycle and multicycle coherent terahertz radiation from relativistic electrons," *Phys. Rev. Lett.*, vol. 107, no. 20, 2011, Art. no. 204801.

[39] M. Dunning *et al.*, "Generating periodic terahertz structures in a relativistic electron beam through frequency down-conversion of optical lasers," *Phys. Rev. Lett.*, vol. 109, no. 7, 2012, Art. no. 074801.

[40] H. Zhang *et al.*, "Coherent terahertz radiation with orbital angular momentum by helically microbunched electron beam," *AIP Adv.*, vol. 11, no. 5, 2021, Art. no. 055115.

[41] A. Weling and D. Auston, "Novel sources and detectors for coherent tunable narrow-band terahertz radiation in free space," *J. Opt. Soc. Amer. B: Opt. Phys.*, vol. 13, no. 12, pp. 2783–2791, 1996.

[42] J. Rosenzweig, G. Travish, and A. Tremaine, "Coherent transition radiation diagnosis of electron beam microbunching," *Nucl. Instruments Methods Phys. Research, Sect. A: Accelerators, Spectrometers, Detectors Assoc. Equip.*, vol. 365, no. 1, pp. 255–259, 1995.

[43] E. Hemsing and J. Rosenzweig, "Coherent transition radiation from a helically microbunched electron beam," *J. Appl. Phys.*, vol. 105, no. 9, 2009, Art. no. 093101.

[44] S. Reiche, "Genesis 1.3: A fully 3D time-dependent fel simulation code," *Nucl. Instruments Methods Phys. Res., Sect. A: Accelerators, Spectrometers, Detectors Assoc. Equip.*, vol. 429, no. 1, pp. 243–248, 1999.